Ab initio calculation of thermodynamic potentials and entropies for superionic water

Martin French,[1] Michael P. Desjarlais,[2] and Ronald Redmer[1]
[1]*Universität Rostock, Institut für Physik, D-18051 Rostock, Germany*
[2]*Sandia National Laboratories, Albuquerque, New Mexico 87185, USA*
(Received 10 September 2015; published 25 February 2016)

We construct thermodynamic potentials for two superionic phases of water [with body-centered cubic (bcc) and face-centered cubic (fcc) oxygen lattice] using a combination of density functional theory (DFT) and molecular dynamics simulations (MD). For this purpose, a generic expression for the free energy of warm dense matter is developed and parametrized with equation of state data from the DFT-MD simulations. A second central aspect is the accurate determination of the entropy, which is done using an approximate two-phase method based on the frequency spectra of the nuclear motion. The boundary between the bcc superionic phase and the ices VII and X calculated with thermodynamic potentials from DFT-MD is consistent with that directly derived from the simulations. Differences in the physical properties of the bcc and fcc superionic phases and their impact on interior modeling of water-rich giant planets are discussed.

DOI: 10.1103/PhysRevE.93.022140

I. INTRODUCTION

Many planetary bodies contain large amounts of water due to the high abundance of oxygen nuclei in protoplanetary discs [1,2]. The thermodynamic states in the interior of our solar water-rich planets, the ice giants Uranus [3] and Neptune [4], range up to pressures of 10 Mbar and temperatures of several thousand degrees Kelvin [5–10]. Under such extreme conditions, water is predicted to form exotic superionic phases characterized by a crystalline oxygen lattice and mobile protons [11–15]. Although a direct experimental proof of the superionic structure is still needed, there is strong indication of its existence by a kink in the melting line of ice VII [16–20]. Furthermore, static [21] and dynamic compression techniques [22,23] were used to measure the conductivity of dense proton-conducting states of water. Theoretical conductivity calculations for superionic water (SIW) can reproduce such measurements with reasonable accuracy [24,25].

In a recent paper, it was predicted that SIW with an fcc oxygen lattice is thermodynamically favored against the phase with a bcc lattice for a wide range of pressures and temperatures [15]. Moreover, it was claimed that the diffusion coefficient of the protons depends significantly on the type of the oxygen lattice, which would have implication on the electrical conductivity and, possibly, the magnetic field generation [10,26] in water-rich giant planets. Even though water never occurs as a pure compound in planetary bodies, its thermophysical properties under extreme conditions need to be well understood before considering more complex planetary mixtures that contain additional elements.

Here we employ finite-temperature density functional theory (FT-DFT) combined with molecular dynamics (MD) simulations to construct analytic free energy functions $f(\varrho,T)$ for the superionic phases with body-centered cubic (bcc) and face-centered cubic (fcc) oxygen lattices. This is achieved by fitting equation of state (EOS) data from the FT-DFT-MD simulations as well as calculating the entropy with a multicomponent two-phase thermodynamic model [27–29].

Having obtained the complete thermodynamic information of the SIW phases, we then investigate the location of transitions between them. The boundary to the dense ices VII and X, for which a corresponding thermodynamic potential is also available [30], is calculated as well. It is in good agreement with that observed directly in the MD simulations.

Finally, we discuss the differences between the thermodynamic properties of the superionic phases. Additional investigations show that the type of the oxygen lattice in SIW has no significant influence on the diffusion coefficient, which is in contrast to the results of Wilson *et al.* [15]. The thermodynamic functions constructed in this work are intended to become part of a wide-range EOS for water in the future.

II. THEORETICAL FOUNDATIONS

This section contains the principal information about the theoretical basics of our work. It is divided into several subsections that present the FT-DFT-MD method in general and various aspects of the procedure used to calculate the entropy.

A. Details of the FT-DFT-MD simulations

Based on the Born-Oppenheimer approximation, our system of electrons, protons, and oxygen nuclei is investigated by performing MD simulations for the heavy particles with forces derived from an FT-DFT treatment of the electrons [31–33] at each time step. The procedure is implemented in the Vienna *ab initio* simulation package (VASP) [34–38]. For given density ϱ and temperature T, one obtains the EOS for the pressure $p_{\mathrm{MD}}(\varrho,T)$, internal energy $u_{\mathrm{MD}}(\varrho,T)$, in addition to various microscopic properties of the electrons and ions.

We use the exchange-correlation functional of Perdew, Burke, and Ernzerhof (PBE) [39] in our FT-DFT-MD calculations. Previous work has shown that thermodynamic properties derived with the PBE functional are in very good agreement with shock-wave experiments that probed extreme states of fluid water [40–44].

The standard PAW pseudopotentials [45,46] provided with VASP (hydrogen PAW-sphere radius: 0.52 Å, oxygen PAW-sphere radius: 0.72 Å) are used with a plane-wave cutoff of 900 eV. All FT-DFT-MD simulations are performed with

particle numbers of at least 54 water molecules and at the Baldereschi **k** point [47]. Using the Baldereschi point ensures excellent convergence of the EOS also in the dense metallic bcc SIW that is comparable to using the $2 \times 2 \times 2$ Monkhorst-Pack grid [48]. This finding is in line with the extensive convergence tests made in previous work [13,14,24]. All simulations are run for 10 000 to 30 000 time steps of length 0.3 fs after equilibration. Relatively long simulation runs are required to reach an excellent statistical accuracy that is necessary to calculate frequency spectra and small pressure differences, which many of our results rely on. The temperature is controlled with a Nosé-Hoover thermostat [49,50].

To calculate the EOS for the bcc SIW, we performed 75 FT-DFT-MD simulations at different densities between 2.25 and 15 g/cm^3 and temperatures between 1500 and 12 000 K in its stability region using 54 molecules. In case of the fcc SIW, we obtained 99 data points at different densities and temperatures with 108 molecules. The fcc SIW generally has a slightly extended stablity regime toward lower temperatures than the bcc SIW. However, it becomes unstable above 13 g/cm^3 at all temperatures, i.e., the oxygen lattice gets distorted, while the bcc SIW can remain stable also beyond 15 g/cm^3.

Additional FT-DFT-MD simulations were made at the 4000 K isotherm to calculate effective partial volumes that are necessary to determine the entropy. Details on those calculations are given in a subsequent section.

B. Frequency spectra of the nuclear motion

The key quantities in the calculation of the entropy from MD simulations are the following spectra of vibrational modes of the nuclei [51]:

$$S_\alpha(\nu) = \frac{4m_\alpha}{3k_BT}\int_0^\infty dt\ \cos(2\pi\nu t)\langle\vec{v}_\alpha(t)\cdot\vec{v}_\alpha(0)\rangle, \quad (1)$$

where m_α is the mass of a nucleus of species α and k_B is Boltzmann's constant. The velocity autocorrelation functions $\langle\vec{v}_\alpha(t)\cdot\vec{v}_\alpha(0)\rangle$ of the species α are calculated from the nuclear motion in the FT-DFT-MD. There is one frequency spectrum per species, formally normalized to

$$\int_0^\infty d\nu\, S_\alpha(\nu) = 1. \quad (2)$$

This condition is satisfied to better than 1% in our simulations.

Apart from entropy calculations, we use the spectra $S_\alpha(\nu)$ to augment the internal energy of our FT-DFT-MD simulations with a quantum correction. This procedure allows us to incorporate nuclear quantum effects, e.g., from molecular vibrations into our EOS data. More precisely, the classical harmonic oscillator energy k_BT is replaced by the respective quantum-statistical value for each frequency interval as follows [51]:

$$u_{vc} = \frac{3}{m}\sum_\alpha N_\alpha\int_0^\infty d\nu\, S_\alpha(\nu) \times\left[h\nu\left(\frac{1}{2}+\frac{1}{\exp(h\nu/k_BT)-1}\right)-k_BT\right]. \quad (3)$$

In the above formula, the total mass of the nuclei is defined as $m = \sum_\alpha N_\alpha m_\alpha$, where N_α is the number of nuclei of species α.

A similar expression can be obtained also for direct calculations of the entropy [51]. However, it is limited to applications to solid systems due to a divergence in the harmonic entropy weighting function at zero frequency.

C. Calculation of the entropy

Calculating the nuclear entropy of fluids from MD simulations with the frequency spectra $S_\alpha(\nu)$ requires an elaborate formalism [27–29]. The respective procedure is based on a separation of the properties of the fluid into a gas-like and a solid-like fraction [27] and was developed by Lin *et al.* [27]. The method involves a description of the gas-like fraction consistently with a hard-sphere model and of the solid-like fraction with the harmonic oscillator model. Later, the formalism was substantially improved by Desjarlais [29], so that an accuracy of better than 0.1 k_B/atom became achievable, which was demonstrated in application to several liquid metals, including calculations of the melting curves of sodium [29] and aluminum [52]. Moreover, the method of Lin *et al.* [27] was also generalized to multicomponent systems, which then requires a more extended treatment in order to derive effective partial volumes of the individual species [28]. In this work, we use the combined extensions by Desjarlais [29] and Lai *et al.* [28] to calculate the entropy of superionic water.

For clarity, we first compile the most important aspects of the formalism in a compact way. For more detailed derivations, we refer the interested reader to the original papers [27–29]. Note that the normalization of our spectra $S_\alpha(\nu)$, differs from that in the former literature, so that the following expressions may carry corresponding prefactors.

Our starting point is the formal separation of the frequency spectra into gas-like, $S^g_\alpha(\nu)$, and solid-like, $S^s_\alpha(\nu)$, parts:

$$S_\alpha(\nu) = f^g_\alpha S^g_\alpha(\nu) + \left(1-f^g_\alpha\right)S^s_\alpha(\nu), \quad (4)$$

where the fluidity factors f^g_α determine the fractions of the gas-like components. The specific entropy then takes the form

$$s_{\rm nuc}(\varrho,T) = \frac{1}{m}\sum_\alpha N_\alpha\int_0^\infty d\nu \times\left[f^g_\alpha S^g_\alpha(\nu)W^g_\alpha + \left(1-f^g_\alpha\right)S^s_\alpha(\nu)W^s_\alpha(\nu)\right]. \quad (5)$$

The weighting function of the solid-like part is taken from the quantum-statistical harmonic oscillator model and reads

$$W^s_\alpha(\nu) = 3k_B\left\{\frac{h\nu/k_BT}{\exp(h\nu/k_BT)-1} - \ln[1-\exp(-h\nu/k_BT)]\right\}. \quad (6)$$

For the gas-like fraction one assumes a weighting function from a hard-sphere model [53],

$$W^g_\alpha = k_B\left\{\frac{S^{IG}_\alpha}{k_B}+\ln\left[\frac{1+\gamma_\alpha+\gamma_\alpha^2-\gamma_\alpha^3}{(1-\gamma_\alpha)^3}\right]+\frac{3\gamma_\alpha^2-4\gamma_\alpha}{(1-\gamma_\alpha)^2}\right\}, \quad (7)$$

where the ideal gas term is

$$\frac{S^{IG}_\alpha}{k_B} = \frac{5}{2}-\ln\left[\left(\frac{h^2}{2\pi m_\alpha k_BT}\right)^{3/2} n^{\rm eff}_\alpha f^g_\alpha\right]. \quad (8)$$

In this multicomponent description [28], special attention has to be paid to the effective particle densities

$$n_\alpha^{\text{eff}} = \frac{N_\alpha}{V_\alpha}. \tag{9}$$

The partial volumes V_α need to be determined separately, which is described in the following section.

The effective hard-sphere packing fractions γ_α are derived by numerically solving the equation [29],

$$\gamma_\alpha^{2/5}\Delta_\alpha^{3/5} = \frac{2(1-\gamma_\alpha)^3}{2-\gamma_\alpha}, \tag{10}$$

for given normalized diffusivities Δ_α. The latter are determined by the zero-frequency value of the spectra in the following way:

$$\Delta_\alpha = \frac{2}{3}S_\alpha(0)\sqrt{\frac{\pi k_B T}{m_\alpha}}\left(n_\alpha^{\text{eff}}\right)^{1/3}\left(\frac{6}{\pi}\right)^{2/3}. \tag{11}$$

At this point, an ansatz for the gas-like spectra $S_\alpha^g(\nu)$ is required. Lin *et al.* [27] chose a Lorentz function, which is characteristic for an uncorrelated system of particles described within the relaxation-time approximation. However, the slow ν^{-2} decay of such Lorentz spectra leads to an overshooting of the total spectra at high frequencies. This has the unphysical consequence that the residual solid-like spectra $S_\alpha^s(\nu)$ become negative. Moreover, the entropies derived with Lorentz spectra are significantly too high [29].

To remedy these problems, correlations need to be included into the gas-like spectra, which can be achieved by using an alternative ansatz derived within a memory function formalism [29,54–56]:

$$S_\alpha^{GK}(\nu) = \frac{2}{\hat{K}_\alpha^{GK}(2\pi\nu i)+2\pi\nu i} + \frac{2}{\hat{K}_\alpha^{GK}(-2\pi\nu i)-2\pi\nu i}. \tag{12}$$

The employment of a Gaussian memory function [57] leads to the following Laplace transform of the kernel [29]:

$$\hat{K}_\alpha^{GK}(z) = \frac{A_\alpha}{2}\sqrt{\frac{\pi}{B_\alpha}}\exp\left(\frac{z^2}{4B_\alpha}\right)\text{erfc}\left(\frac{z}{2\sqrt{B_\alpha}}\right), \tag{13}$$

where $\text{erfc}(x)$ is the complementary error function. The constants A_α are given by

$$A_\alpha = \frac{4B_\alpha}{2+\sqrt{\pi\left(1+\frac{B_\alpha S_\alpha^2(0)}{4\gamma_\alpha^{4/5}\Delta_\alpha^{6/5}}\right)}}. \tag{14}$$

The remaining parameters B_α are formally determined by moments of the spectra $S_\alpha(\nu)$ [29]. In practice, the B_α are obtained by manually matching the high-frequency tail of $S_\alpha^{GK}(\nu)$ with that of the $S_\alpha(\nu)$, which is a much more efficient way.

The fluidity factors to be used in the above expressions then read

$$f_\alpha^g = f_\alpha^{GK} = \frac{A_\alpha S_\alpha(0)}{8}\sqrt{\frac{\pi}{B_\alpha}}, \tag{15}$$

and they differ from those one would obtain with Lorentzian gas-like spectra [27].

Note that for all nuclear species α that are immobile (like the oxygen in superionic water) the gas-like fraction is $f_\alpha = 0$. The treatment of the respective contribution to the nuclear entropy is then performed purely with the harmonic-oscillator weighting functions [51]. Consequently, no ideal-mixing contribution to the entropy [28] is added here because there is only a single fluid component (hydrogen) in the MD. Therefore, for our special case of SIW, which has two species but no mixing, we must multiply V_H by N/N_H in the ideal gas contribution to the hydrogen entropy, Eq. (8), in order to preserve the correct ideal gas limit, where $V_H/N_H = V_O/N_O = V/N$.

Furthermore, we do not take into account the nuclear spin or isotopic entropies here. Those are not required for our purpose of calculating phase boundaries because the composition of nuclear species is conserved.

Last, the electronic contribution to the specific entropy is derived from the Fermi occupation numbers f_i of the electronic states from the DFT [33]:

$$s_{\text{el}}(\varrho,T) = -\frac{k_B}{m}\left\langle\sum_i\left[f_i\ln f_i + (1-f_i)\ln(1-f_i)\right]\right\rangle. \tag{16}$$

The total specific entropy of our system then reads

$$s_{\text{tot}}(\varrho,T) = s_{\text{nuc}}(\varrho,T) + s_{\text{el}}(\varrho,T). \tag{17}$$

Obviously, the method employed here is approximate, and there is no guarantee that it will produce results as accurate as coupling-constant integration methods [58,59] may yield. On the other hand, its complexity scales only linearly in dependence of the number of nuclear species. Another advantage is the capability to capture nuclear quantum effects in the entropy, which enter via the weighting function of the solid-like component. This allows us to consistently calculate phase boundaries with solids described by a realistic EOS containing quantum effects of the nuclear motion.

D. Calculation of the effective partial volumes

The partial volumes that enter Eq. (9) are crucial quantities in entropy calculations from MDs with different nuclear species. They are defined as [28]

$$V_\alpha = N_\alpha\left(\frac{\partial V}{\partial N_\alpha}\right)_{p,T,\{N_\beta\}} = N_\alpha\xi_\alpha. \tag{18}$$

The total volume of the system is given by $V = \sum_\alpha V_\alpha$. With the help of the scaling quantities ξ_α, which correspond to the mean volume per particle of species α, Eq. (9) can be recast into the convenient form

$$n_\alpha^{\text{eff}} = \frac{N_\alpha}{V_\alpha} = \frac{1}{V\xi_\alpha}\sum_\beta N_\beta\xi_\beta. \tag{19}$$

That way, we easily observe that it is sufficient to determine only the ratios ξ_β/ξ_α in the multicomponent case. We do not rely on simple estimations for the ξ_α for the extreme conditions of interest here, but instead calculate them directly with the FT-DFT-MD method.

The ξ_α can theoretically be calculated by inserting or removing very few particles i_α or j_α of the respective species from the FT-DFT-MD simulations of standard composition at

constant pressure and temperature:

$$\xi_\alpha = \left(\frac{\Delta V}{\Delta N_\alpha}\right)_{p,T,\{N_\beta\}} = \frac{V(p,T,N_\alpha + i_\alpha,\{N_\beta\}) - V(p,T,N_\alpha - j_\alpha,\{N_\beta\})}{i_\alpha + j_\alpha}. \tag{20}$$

Ideally, one would choose both $i_\alpha = j_\alpha = 1$. In order to circumvent the adjustment of the pressure in DFT-MD simulations, we use the following transformation

$$\left(\frac{\partial V}{\partial N_\alpha}\right)_{p,T,\{N_\beta\}} = -\left(\frac{\partial p}{\partial N_\alpha}\right)_{V,T,\{N_\beta\}} \left(\frac{\partial V}{\partial p}\right)_{T,N_\alpha,\{N_\beta\}} = \frac{V}{K_T}\left(\frac{\partial p}{\partial N_\alpha}\right)_{V,T,\{N_\beta\}}, \tag{21}$$

where the isothermal bulk modulus,

$$K_T = -V\left(\frac{\partial p}{\partial V}\right)_{T,N_\alpha,\{N_\beta\}} = \varrho\left(\frac{\partial p}{\partial \varrho}\right)_{T,N_\alpha,\{N_\beta\}}, \tag{22}$$

is introduced. For small changes in composition of the fluid, we can then write

$$\xi_\alpha = \frac{V}{K_T}\left(\frac{\Delta p}{\Delta N_\alpha}\right)_{V,T,\{N_\beta\}} = \frac{V}{K_T}\frac{p(V,T,N_\alpha + i_\alpha,\{N_\beta\}) - p(V,T,N_\alpha - j_\alpha,\{N_\beta\})}{i_\alpha + j_\alpha}. \tag{23}$$

One can eliminate the bulk modulus and obtain a simple expression for the desired ratios:

$$\frac{\xi_\beta}{\xi_\alpha} = \left(\frac{\Delta p}{\Delta N_\beta}\right)_{V,T,N_\alpha,\{N_\gamma\}} \left(\frac{\Delta N_\alpha}{\Delta p}\right)_{V,T,N_\beta,\{N_\gamma\}}. \tag{24}$$

The above equation only requires the calculation of the pressure differences with few DFT-MD simulations in the NVT ensemble with inserted or removed particles. It is very convenient to use for multicomponent fluid systems.

However, in the case of superionic water, it is not possible to insert or remove an oxygen atom from the lattice without distorting it, which would lead to discontinuous changes in the thermodynamic functions. Instead, we directly use Eq. (18) and write

$$\frac{\xi_\beta}{\xi_\alpha} = \frac{V_\beta}{N_\beta}\frac{N_\alpha}{V_\alpha}. \tag{25}$$

For a system with only two nuclear species, the following expression can be easily derived using some of the above relations:

$$\frac{\xi_\beta}{\xi_\alpha} = \frac{N_\alpha}{N_\beta}\frac{V - V_\alpha}{V_\alpha} = \frac{N_\alpha}{N_\beta}\left[\frac{V}{N_\alpha}\left(\frac{\Delta N_\alpha}{\Delta V}\right)_{p,T,N_\beta} - 1\right]. \tag{26}$$

We can once more use Eq. (21) and find the result:

$$\frac{\xi_\beta}{\xi_\alpha} = \frac{N_\alpha}{N_\beta}\left[\frac{K_T}{N_\alpha}\left(\frac{\Delta N_\alpha}{\Delta p}\right)_{V,T,N_\beta} - 1\right]. \tag{27}$$

This expression does not contain any differences ΔN_β (here oxygen). It requires the isothermal bulk modulus $K_T(\varrho,T)$ instead, which can be derived from the EOS straightforwardly.

III. CONSTRUCTION OF THE THERMODYNAMIC POTENTIALS

In this section, we use our EOS and entropy calculations to derive free-energy functions for the bcc and fcc SIW. The EOS of SIW is very similar to that of a dense fluid and cannot be divided into cold curves and thermal parts, as is usually done for crystalline solids [60]. For each phase, the resulting expressions are composed of main parts $f_m(\varrho,T)$ and nuclear quantum correction parts $f_{\rm qc}(\varrho,T)$ in the following way:

$$f(\varrho,T) = f_m(\varrho,T) + f_{\rm qc}(\varrho,T). \tag{28}$$

The entropy constants, although determined in a separate final step of the procedure, are included in the main parts for convenience.

Note that we aim to reach a high precision for the $f(\varrho,T)$ here because the differences in the thermodynamic functions between the bcc and the fcc SIW are small. In numbers, the pressures differ only by about one percent or less, while the internal energies are typically different by no more than 0.5 kJ/g.

A. Main contribution from the FT-DFT-MD

The indispensible requirement for the construction of a thermodynamic potential from MD simulations is the availability of very well converged EOS data. Our basic EOS quantities are the pressure $p_{\rm MD}(\varrho,T)$ and the internal energy $u_{\rm MD}(\varrho,T)$. In SIW, both quantities increase almost linearly with the temperature. Most noteworthy, both $u_{\rm MD}(\varrho,T)$ and the reduced pressure $p_{\rm MD}(\varrho,T)/\varrho$ show a fairly linear increase with the density in the strongly compressed region between 10 and 15 g/cm^3. Both quantities are displayed in Fig. 1. Such a quasilinear dependence on the density is not an uncommon observation for warm dense matter in an intermediate region of compression [61–63], i.e., between the energy minimum at ambient conditions and the Thomas-Fermi limit.

Having these general considerations in mind, we make the following generic ansatz for the free-energy function:

$$\begin{aligned} f_m(\varrho,T) = &\sum_{ik} \alpha_{ik} T^{i/i_0} \varrho^{k/k_0} + \sum_{il} \beta_{il} T^{i/i_0} L_\varrho^l \\ &+ \sum_{jk} \gamma_{jk} L_T^j \varrho^{k/k_0} + \sum_{jl} \delta_{jl} L_T^j L_\varrho^l \\ &+ \sum_{k} \varepsilon_k T \ln(T + T_0) \varrho^{k/k_0} \\ &+ \sum_{l} \omega_l T \ln(T + T_0) L_\varrho^l, \end{aligned} \tag{29}$$

where i_0 and k_0 are preset suppressor constants and the modified logarithms are defined as

$$L_\varrho = L_\varrho(l) = \ln[\varrho + (l-1)\varrho_0] \tag{30}$$

and

$$L_T = L_T(j) = \ln(T + jT_0). \tag{31}$$

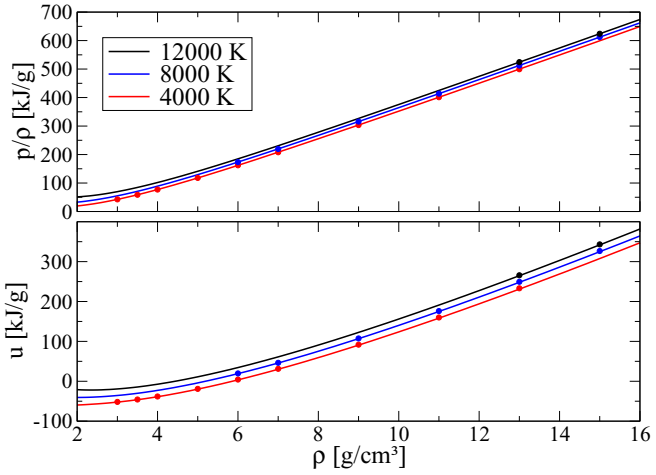

FIG. 1. Three isotherms of the reduced pressure $p_{\mathrm{MD}}(\varrho,T)/\varrho$ (top panel) and the internal energy $u_{\mathrm{MD}}(\varrho,T)$ (bottom panel) for bcc SIW. The circles indicate the data from the FT-DFT-MD simulations while the lines are the results from the fits Eqs. (32) and (33). The temperatures are 12 000 K (black upper line), 8000 K (blue middle line), and 4000 K (red lower line). Results for the fcc SIW are not shown here because they would be mostly on top of that from the bcc SIW.

The smoothing constants ϱ_0 and T_0 serve to remove unwanted logarithmic divergences at low values and are also preset. The indexes j and l may run over positive integers, while the i and k may be any set of positive or negative integers. The quantities α_{ik}, β_{il}, γ_{jk}, δ_{jl}, ε_k, and ω_l are parameters to be determined in an automatic fitting procedure.

Analytic expressions for our quantities of principal interest are easily obtained by differentiation. These are the reduced pressure

$$\frac{p_m(\varrho,T)}{\varrho} = \varrho\left(\frac{\partial f_m}{\partial \varrho}\right)_T, \tag{32}$$

and the internal energy

$$u_m(\varrho,T) = -T^2\left(\frac{\partial (f_m/T)}{\partial T}\right)_\varrho, \tag{33}$$

which are of same dimension as the free energy.

The ansatz Eq. (29) allows us to ensure that both the high-density and the high-temperature limits are determined by few terms containing the highest *power* of ϱ and $T\ln T$ (or the highest *power* of T if $i_{\max} > i_0$), respectively. In addition, complex nonlinearities in the EOS can be captured by several terms containing *powers of the modified logarithms*. Those terms are slowly varying functions and contribute only at less extreme conditions of density and temperature. In our particular cases of SIW, the natural choices for tuning the suppressor constants are $i_0 = i_{\max}$ and $k_0 = k_{\max}$. The smoothing constants are set to $\varrho_0 = 1\ \mathrm{g/cm^3}$ and $T_0 = 100\ \mathrm{K}$.

The fitting of the remaining parameters is then performed by formulating a linear optimization problem to simultaneously minimize the least-squares differences to all EOS data points for the reduced pressure Eq. (32) and internal energy Eq. (33), which can be solved numerically. One more important peculiarity to pay attention to is the term $\alpha_{i_0,0}T$. It is directly tied to the absolute entropy and cannot be obtained this way because the term disappears in both Eqs. (32) and (33). The parameter $\alpha_{i_0,0}$ must be separately determined from the entropy calculations, which is done in Sec. III C.

Fits of both excellent fidelity and reasonable behavior in extrapolation beyond the stability regions are achieved for both phases of SIW, which is illustrated in Fig. 1. In numbers, the mean deviation between the fit and the pressure data is less than 0.1%, while the internal energies are on average reproduced to better than 0.1 kJ/g. This is yet somewhat larger than the statistical uncertainties or those that stem from numerical convergence parameters. Further reduction of these deviations would have been possible by including additional higher-order terms. However, it would also have worsened the extrapolation behavior of the functions and inflated the number of coefficients to handle. Therefore, the series were truncated at, e.g., $l_{\max} = 4$ for bcc and $l_{\max} = 5$ for fcc SIW because the EOS data set of the latter phase includes slightly pronounced curvatures. The fit coefficients are given in Table I. For convenience, we also include the coefficient $\alpha_{i_0,0}$ here, albeit that one is determined from the entropy calculations described below.

To conclude this subsection, we note that the ansatz Eq. (29) is of general usefulness for warm dense matter, e.g., dense fluids with a similarly shaped EOS, which we checked in a number of tests with other materials [63–65]. With few modifications, i.e., leaving out the term containing ω_1 and setting $k_0 = 3k_{\max}/2$ and $i_0 = i_{\max}$, it is possible to achieve compatibility with both the Thomas-Fermi and the classical ideal gas limits. A combination with additional terms that describe EOS behavior at low densities [66], which is characterized by various thermal dissociation and ionization processes, seems achievable as well.

B. Nuclear quantum correction

Quantum effects of the nuclear motion cannot be neglected when calculating the thermodynamic properties of SIW. Equation (3) allows us to include such effects at the same level as was recently done for the ices VII and X [30] or earlier calculations for fluid water [44,67]. In the case of fluid ammonia, it was shown that the method can capture effects of thermal dissociation that lead to an increased decay of the nuclear quantum effects due to the loss of intramolecular modes of vibration [61].

Here we investigate strongly correlated, compressed systems at moderate temperatures, which roughly correspond to the characteristic vibrational temperatures of water molecules or phonons in ice. Although the compression of fluid water leads to dissociation of molecular bonds and formation of SIW, the effective vibrational frequencies in the system start to increase again near 3 $\mathrm{g/cm^3}$ due to the reduction of available configuration space. Beyond about 5 $\mathrm{g/cm^3}$, $u_{vc}(\varrho,T)$ in SIW surmounts the values one obtains from characteristic frequencies of isolated water molecules [44]. Figure 2 shows the results obtained with Eq. (3). Differences between the bcc and fcc phases occur only in the dense region and are especially visible below 8000 K. Although the nuclear quantum correction is a relatively small contribution to the EOS, it needs to be treated with the same care as the main part.

TABLE I. Coefficients α_{ik}, β_{il}, γ_{jk}, δ_{jl}, ε_k, and ω_l used in Eqs. (29), (32), and (33) for bcc and fcc SIW. All units are chosen in a way that entering the temperature in K and the density in g/cm^3 leads to results for $f_m(\varrho,T)$ in kJ/g. The remaining constants are $k_0 = 1$, $\varrho_0 = 1$ g/cm^3, and $T_0 = 100$ K for both phases.

Coefficient	bcc	fcc
$i_0 = i_{\max}$	1	2
$\alpha_{0,0}$	$-3.63984992 \times 10^{2}$	$-1.62279576 \times 10^{4}$
$\alpha_{0,1}$	1.43364427×10^{3}	7.42720416×10^{4}
$\alpha_{1,0}$	$1.25922368 \times 10^{-2}$	$-4.03568116 \times 10^{2}$
$\alpha_{1,1}$	$1.97035631 \times 10^{-1}$	1.85798837×10^{3}
$\alpha_{2,0}$	–	9.44227280×10^{0}
$\alpha_{2,1}$	–	$-4.33817146 \times 10^{1}$
$\beta_{0,1}$	$-3.56056653 \times 10^{2}$	$-2.27104207 \times 10^{4}$
$\beta_{0,2}$	$-1.44298289 \times 10^{3}$	$-2.05737109 \times 10^{4}$
$\beta_{0,3}$	5.59430175×10^{2}	$-3.95998221 \times 10^{4}$
$\beta_{0,4}$	$-3.08323312 \times 10^{2}$	1.33150358×10^{4}
$\beta_{0,5}$	–	$-4.09804698 \times 10^{3}$
$\beta_{1,1}$	$-1.43320849 \times 10^{-1}$	$-5.62582310 \times 10^{2}$
$\beta_{1,2}$	$-8.82509173 \times 10^{-2}$	$-5.40915927 \times 10^{2}$
$\beta_{1,3}$	$3.29148647 \times 10^{-2}$	$-9.56594334 \times 10^{2}$
$\beta_{1,4}$	$-3.74794358 \times 10^{-2}$	3.17811925×10^{2}
$\beta_{1,5}$	–	$-1.00389467 \times 10^{2}$
$\beta_{2,1}$	–	1.29955635×10^{1}
$\beta_{2,2}$	–	1.33967031×10^{1}
$\beta_{2,3}$	–	2.13900668×10^{1}
$\beta_{2,4}$	–	$-7.01319766 \times 10^{0}$
$\beta_{2,5}$	–	2.28766744×10^{0}
$\gamma_{1,0}$	3.35489536×10^{1}	3.50463307×10^{3}
$\gamma_{1,1}$	$-1.88285213 \times 10^{2}$	$-1.61345494 \times 10^{4}$
$\delta_{1,1}$	5.58962773×10^{1}	4.93435639×10^{3}
$\delta_{1,2}$	1.72141931×10^{2}	4.46724428×10^{3}
$\delta_{1,3}$	$-6.74546340 \times 10^{1}$	8.58645314×10^{3}
$\delta_{1,4}$	4.08435200×10^{1}	$-2.88082484 \times 10^{3}$
$\delta_{1,5}$	–	8.88638310×10^{2}
ε_0	$-3.37183530 \times 10^{-3}$	$-7.63424649 \times 10^{-1}$
ε_1	$-1.73302844 \times 10^{-2}$	3.49923831×10^{0}
ω_1	$1.42836268 \times 10^{-2}$	$-1.04708374 \times 10^{0}$
ω_2	$6.32756867 \times 10^{-3}$	$-1.09013426 \times 10^{0}$
ω_3	$-2.33253788 \times 10^{-3}$	$-1.71244862 \times 10^{0}$
ω_4	$3.22127559 \times 10^{-3}$	$5.59947252 \times 10^{-1}$
ω_5	–	$-1.83720236 \times 10^{-1}$

We do not have an expression analogous to Eq. (3) to obtain a corresponding pressure correction from the FT-DFT-MD simulations [68]. Nevertheless, it is possible to parametrize a meaningful quantum-correction free-energy function solely from the data for $u_{vc}(\varrho,T)$ when making the following ansatz:

$$f_{\rm qc}(\varrho,T) = \sum_k \eta_k T\left[\ln(1-e^{-T_E/T}) + \ln\left(\frac{T+T_1}{T_E}\right)\right]\varrho^{k/k_0} + \sum_l \zeta_l T\left[\ln(1-e^{-T_E/T}) + \ln\left(\frac{T+T_1}{T_E}\right)\right]\Lambda_\varrho^l + \sum_k \lambda_k \varrho^{k/k_0} + \sum_l \kappa_l \Lambda_\varrho^l. \quad (34)$$

The idea behind Eq. (34) is to have its temperature dependence determined by harmonic oscillator correction functions (with

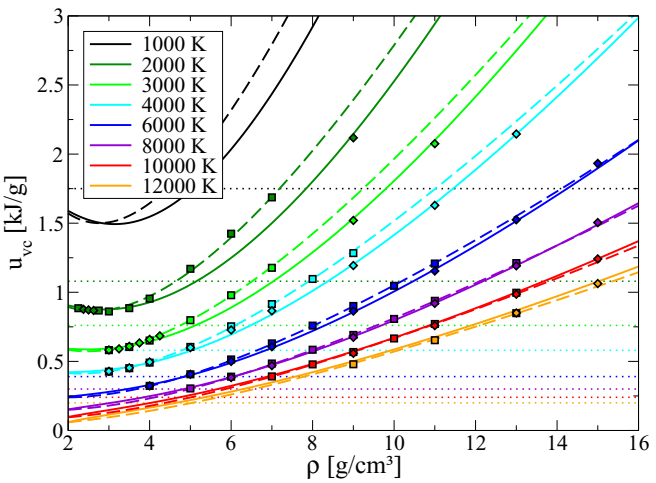

FIG. 2. Isotherms of the quantum correction to the internal energy from Eq. (3). Diamonds are results for bcc and squares for fcc SIW, respectively. The solid and dashed lines are generated with the fit Eq. (36) for bcc and fcc SIW, respectively. The thin dotted lines are values from characteristic frequencies of isolated water molecules [44]. All sets of curves and symbols behave systematically with the temperature indicated in the legend. The highest curves correspond to the lowest temperature, etc., see color code in the online version.

removed low-temperature divergences). It turns out that a single characteristic temperature T_E is sufficient to produce excellent fits to the data. In the high-temperature limit, $f_{\rm qc}(\varrho,T)$ converges to a small constant value, which vanishes against the main contribution $f_m(\varrho,T)$. The density dependence is of similar generic form as that of the main part, Eq. (29), but with somewhat simpler logarithmic terms,

$$\Lambda_\varrho = \ln(\varrho + \varrho_0), \quad (35)$$

that always approach constant values at low densities.

The corresponding expression for the internal energy is obtained by differentiation of Eq. (34), and it contains exactly the same parameters:

$$u_{\rm qc}(\varrho,T) = -T^2\left(\frac{\partial(f_{\rm qc}/T)}{\partial T}\right)_\varrho = \sum_k \eta_k\left(\frac{T_E}{e^{T_E/T}-1} - \frac{T^2}{T+T_1}\right)\varrho^{k/k_0} + \sum_l \zeta_l\left(\frac{T_E}{e^{T_E/T}-1} - \frac{T^2}{T+T_1}\right)\Lambda_\varrho^l + \sum_k \lambda_k \varrho^{k/k_0} + \sum_l \kappa_l \Lambda_\varrho^l. \quad (36)$$

After setting the basic parameters to $k_0 = 1$, $\varrho_0 = 1$ g/cm^3, $T_1 = 100$ K and preoptimizing the characteristic temperature to a value of $T_E = 4500$ K, the parameters η_k, ζ_l, λ_k, and κ_l were fitted with an automatic routine. The fit curves are included in Fig. 2, and they reproduce most of the data within about 0.01 kJ/g, which is a negligible source of error. The fits behave very reasonably also in extrapolation. Table II contains the numerical values of the optimized parameters.

TABLE II. Coefficients η_k, ζ_l, λ_k, and κ_l used in Eqs. (34) and (36) for bcc and fcc SIW. All units are chosen in a way that entering the temperature in K and the density in g/cm^3 leads to results for $f_{\rm qc}(\varrho,T)$ in kJ/g. The remaining constants are $k_0 = 1$, $\varrho_0 = 1$ g/cm^3, $T_E = 4500$ K, and $T_1 = 100$ K for both phases.

Coefficient	bcc	fcc
η_0	$1.66311177 \times 10^{-3}$	$2.48398711 \times 10^{-3}$
η_1	$1.27391534 \times 10^{-3}$	$9.66256285 \times 10^{-4}$
ζ_1	$-8.43618254 \times 10^{-4}$	$-2.16049076 \times 10^{-3}$
ζ_2	$-1.62214854 \times 10^{-3}$	$-6.05171608 \times 10^{-4}$
λ_0	3.09204756	4.97616755
λ_1	2.75926296	2.09621409
κ_1	−1.43268130	−4.39664120
κ_2	−3.56990330	−1.35920623

The corresponding pressure, $p_{\rm qc} = \varrho^2(\partial f_{\rm qc}/\partial\varrho)_T$, amounts to less than 1% of that of the FT-DFT-MD simulations, $p_{\rm MD}(\varrho,T)$, in most cases. It becomes more significant only for the cool and dense states of SIW.

C. Entropy constant

In the previous subsections, we have accomplished the parametrization the thermodynamic potentials $f(\varrho,T)$ for SIW with the exception of the entropy constants $s_0 = \alpha_{i_0,0}$ in Eq. (29), so that the relative behavior of the entropy,

$$s(\varrho,T) = -\left(\frac{\partial f}{\partial T}\right)_\varrho = -\left(\frac{\partial (f_m + f_{\rm qc})}{\partial T}\right)_\varrho , \qquad (37)$$

is already fixed. In principle, a single calculation of the entropy for each phase of SIW would now be sufficient to complete the construction of their thermodynamic potentials. In order to examine the performance of the elaborate formalism to determine the entropy from the FT-DFT-MD simulations (see Sec. II C), we calculate it for several states at the 4000 K isotherm.

The first step is the determination of the volume weighting ratios ξ_O/ξ_H. The only way to accomplish this for SIW is via Eq. (27) because it is not possible to insert or remove oxygen atoms without destroying its lattice. Moreover, we found out that inserting hydrogen atoms in simulation boxes for either phase of SIW leads to a deformation of the oxygen lattices as well. The removal of hydrogen atoms is the only possible way to obtain a smooth derivative of pressure by the particle number N_H, which is required to evaluate Eq. (27). In particular, we removed 2 hydrogen atoms out of 108 from the bcc SIW and 2 out of 216 from the fcc phase, respectively, at constant volume. We verified that the decrease in the pressure is linear for such small changes of N_H with additional test simulations in which only 1 or 4 hydrogen atoms were removed. The bulk moduli were calculated via Eq. (22) using the analytically parametrized EOS for SIW.

The results for ξ_O/ξ_H along the 4000 K isotherm are shown in the lower panel of Fig. 3, and there are significant differences between the fcc and bcc phases of SIW. In the fcc phase, the ratio takes a density-independent value of $\xi_O/\xi_H \approx 3.7$ for all densities at which the fcc lattice structure is dynamically stable, i.e., up to 9 g/cm^3. In bcc SIW, the effective volume

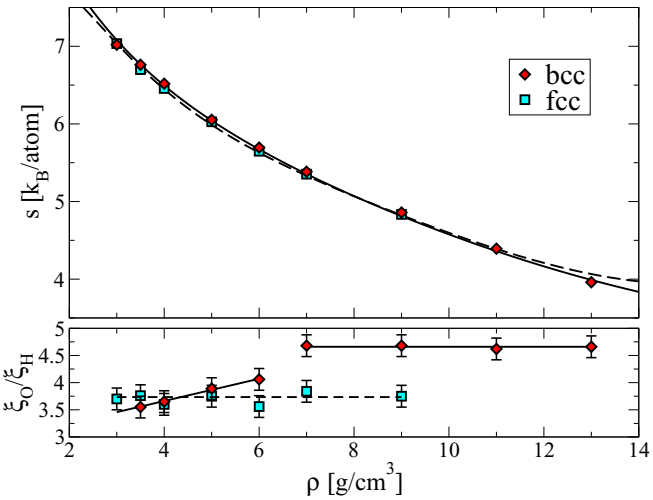

FIG. 3. Top panel: Calculated entropy for bcc and fcc SIW at 4000 K, represented by diamonds and squares, respectively. The solid and dashed lines are the results from the fit formula, Eq. (29), for the bcc and fcc phases, respectively. Bottom panel: Calculated ratios ξ_O/ξ_H for the same states as in the top panel. The lines are simple linear fits to the data.

of a hydrogen atom shrinks significantly under compression compared to that of an oxygen atom. This can be understood with the rearrangement of the protons, which relocate from ice X positions into octahedreal sites under compression [14]. This rearrangement allows the system to yield internally and, thus, to stabilize its structure up to high densities far beyond 15 g/cm^3. It has a very pronounced effect on the ξ_O/ξ_H ratio in bcc SIW up to 7 g/cm^3, albeit it is not discontinuous. The lines drawn in the lower panel of Fig. 3 are guides to the eye. The rearrangement of protons is also accompanied by a metallization transition [24]. Electron-proton pair correlation functions show a delocalization of electrons with increasing density [24]. No such proton rearrangement or metallization happens in the fcc phase.

The uncertainty in the ratios ξ_O/ξ_H amounts to 5% or less for each individual calculation. To further suppress this source of error, we use the values from the simple fits displayed as lines in the lower panel of Fig. 3 when calculating the entropy $s_{\rm tot}(\varrho,T)$. This also enables us to calculate the entropy at 3 g/cm^3, for which ξ_O/ξ_H cannot be determined directly because the oxygen lattice melts when removing hydrogen at that low density. All in all, the entropy is not very sensitive to the ratio of effective volumes. An error of 5% in ξ_O/ξ_H causes an entropy error of less than 0.01 k_B/atom.

The entropy calculated at the 4000 K isotherm is shown in the upper panel of Fig. 3. It decreases with the density for both phases of SIW. The entropy of the bcc phase is roughly 0.04 k_B/atom higher than that of the fcc phase at most of the densities. It is now easy to fit the final coefficients $\alpha_{i_0,0}$ from Eq. (29) by shifting the respective entropy functions and match them with the calculated data. The average deviation between the fits and each individual data point is less than 0.03 k_B/atom, which is approximately the statistical accuracy that our entropy calculations are converged to. From such good consistency between the entropy functions $s(\varrho,T)$ derived from the EOS

data and the directly calculated numbers, we can expect the absolute values of the entropy to be accurate within the same degree of uncertainty.

IV. PHASE DIAGRAM AND TRANSITIONS TO THE ICES VII AND X

Having obtained the complete thermodynamic information for the bcc and fcc SIW, we can now use Eq. (28) to calculate the free enthalpies,

$$g(\varrho,T) = f(\varrho,T) + \varrho\left(\frac{\partial f}{\partial \varrho}\right)_T, \tag{38}$$

which are numerically inverted into the form $g(p,T)$ using the pressures $p(\varrho,T) = \varrho^2(\partial f/\partial\varrho)_T$. Boundaries between two phases are found by calculating the intersection of the respective free enthalpies via $\Delta g(p,T) = 0$.

A phase diagram of warm dense water is displayed in Fig. 4. It includes the data points for which dynamically stable FT-DFT-MD simulations were obtained for the bcc and fcc phases SIW. Additional points for the fluid as well as for the ices VII* and X were taken from previous work [14,30]. The calculated phase boundary between bcc and fcc SIW (solid green line) is located in the center of their dynamic stability regions, whereas the fcc SIW is thermodynamically favored below the curve. The characteristic density jump at this boundary is small. For example, at 4000 K it amounts to 0.3% at 240 GPa and 0.14% at 4900 GPa.

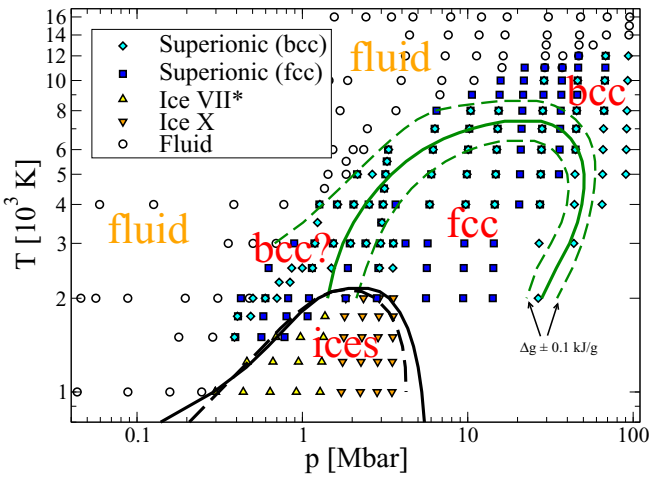

FIG. 4. Phase diagram of warm dense water. Diamonds and squares indicate FT-DFT-MD simulation points for the superionic phases with bcc and fcc lattices, respectively, made in this work. Additional data for the ices VII* and X (triangles) as well as for the fluid (circles) were taken from Refs. [30] and [14]. The solid green line (gray in print version) is the phase boundary between the bcc and fcc phases of SIW derived using the thermodynamic potentials, Eq. (28). The dashed green lines (gray in print version) are corresponding boundaries, but were obtained after adding artificial energy differences of ± 0.1 kJ/g to $\Delta g(p,T)$. The solid and dashed black lines are the boundaries between the bcc and fcc SIW, respectively, and the ices, for which the thermodynamic potential was taken from Ref. [30].

To examine the sensitivity of this boundary against uncertainties in the thermodynamic potentials, we also calculate it after adding small offsets of ± 0.1 kJ/g to $\Delta g(p,T)$, which shifts the boundary significantly. It is very difficult to estimate the actual uncertainty of $\Delta g(p,T)$, but it is likely to be larger than 0.1 kJ/g. Therefore, we cannot precisely determine up to which degree each of the phases of SIW may be present in the phase diagram. However, it is certain that the bcc phase will eventually prevail against the fcc phase toward high pressures. This result is also concordant with the loss of dynamic stability of fcc SIW there. The fcc phase is likely to vanish against bcc SIW also at high temperatures, albeit we cannot say if this happens below or above the transition between bcc SIW and the fluid phase. The fcc phase certainly prevails in a region of order 10 Mbar and few 1000 K.

In a previous paper [30], we constructed a single-phase thermodynamic potential for ices VII* and X, using FT-DFT-MD simulations on the same level of approximation as here (PBE XC-functional, derivation of the entropy from power spectra [51]). A multistage fitting procedure was employed to fit energy and entropy data calculated from MD simulations to an analytic free-energy function suited model the thermodynamics of a solid. The numerical accuracy of that fit was comparable to that achieved here, i.e., residual deviations in internal energy amounted to about 0.1 kJ/g.

The respective boundaries between each of the phases of SIW and the ices VII* and X are displayed in Fig. 4 as well. The ices have a bcc oxygen lattice, and their protonic structures can melt upon heating, so that the transtion to bcc SIW is directly observable in simulations. The calculated boundary between bcc SIW and the ices (solid black line) is located relatively well between the data points that represent the dynamically stable states of both ices and bcc SIW. Nevertheless, it lies somewhat low in temperature and touches some of the highest data points of the ices. A plausible explanation for this is that the ion dynamics in the FT-DFT-MD simulations is purely classical, whereas our thermodynamic potentials contain nuclear quantum effects via the postprocessing correction of the internal energy data with power spectra; see Eq. (3) or Sec. III B. If such quantum effects were inherent in the MD simulations, it would very likely result in a lower melting temperature of the proton sublattice because potential barriers can be overcome more easily by quantum particles. The dynamic stability regime of fcc SIW partially overlaps with that of the ices because the shape of the simulation cell is kept fixed in our simulations, so that a direct transition between those two phases is not possible. The calculated boundary (dashed black line) is close to that between the ices and bcc SIW though. This illustrates again the strong similarity that both phases of SIW share in their thermodynamic functions. A likewise investigation of sensitivity of the SIW-to-ice transitions shows that their shifts are one order of magnitude smaller compared to that of the bcc-fcc transition line when adding ± 0.1 kJ/g to $\Delta g(p,T)$.

There have been several predictions of crystalline structures of water ice at zero Kelvin beyond the stability region of ice X [69–75]. Those ices may have boundaries to SIW, but most of them are of noncubic structure and the derivation of accurate thermodynamic potentials for them is not an easy task. Similarly, the calculation of the transitions between SIW and the fluid phase would require the construction of

TABLE III. Diffusion coefficients of the protons in cm^2/s for bcc and fcc SIW.

T [K]	ϱ[g/cm^3]	bcc	fcc
4000	3.0	1.24×10^{-3}	1.26×10^{-3}
4000	3.5	1.23×10^{-3}	1.24×10^{-3}
4000	4.0	1.20×10^{-3}	1.22×10^{-3}
4000	5.0	1.12×10^{-3}	1.08×10^{-3}
4000	6.0	9.60×10^{-4}	9.78×10^{-4}
4000	7.0	7.86×10^{-4}	8.36×10^{-4}
4000	9.0	5.35×10^{-4}	5.64×10^{-4}
5000	5.0	1.53×10^{-3}	1.45×10^{-3}
5000	7.0	1.05×10^{-3}	1.12×10^{-3}
5000	9.0	6.96×10^{-4}	7.75×10^{-4}

a thermodynamic potential for the fluid phase. Although this should be achievable using the same techniques as here, it is out of scope of this work.

V. PROTON DIFFUSION IN SUPERIONIC WATER

Although the thermodynamic properties of bcc and fcc SIW are very similar, their transport properties might differ. Wilson *et al.* reported a significant effect of the type of oxygen lattice on the proton diffusion coefficients [15]. We have calculated the self-diffusion coefficients of the protons, D_H, from our FT-DFT-MD simulations using the velocity auto-correlation functions:

$$D_\alpha = \frac{1}{3}\int_0^\infty dt\, \langle \vec{v}_\alpha(t) \cdot \vec{v}_\alpha(0) \rangle = \frac{k_B T}{4 m_\alpha} S_\alpha(0). \qquad (39)$$

In contrast to the results of Wilson *et al.*, we do not observe a significant difference in the proton diffusion coefficients within the statistical error of 5% or less. At the very most, the values for the fcc phase tend to be up to 10% larger than that for bcc SIW, and this occurs only for densities larger than 6 g/cm^3. Table III contains the respective values along the 4000 K isotherm, for which we have produced the longest simulations (about 10 ps) in order to calculate the entropy, plus three values at 5000 K from shorter simulations. These states include all those for which diffusion coefficients were given in Ref. [15], with the exception of the data at the 2000 K isotherm and at 11 g/cm^3 and 5000 K. At those conditions, we observed a distortion of either the bcc or the fcc lattices, i.e., a dynamic instability of one of the phases in the simulations.

Our values fit very well into a set of previous results for bcc SIW obtained with the mean-square-displacement method and follows the same trends with temperature and density [24]. Strangely, the absolute values for the diffusion coefficients given by Wilson *et al.* are about two orders of magnitude higher than ours. Such high values of D_H would lead to unrealistically high ionic electrical conductivities of order 10^5 to 10^6 S/m, which is a characteristic number rather for electronic transport in dense plasmas [76].

Since the type of the oxygen lattice does not strongly affect the proton diffusion, it is unlikely that related ionic transport properties, e.g., the electrical conductivity [25], are significantly influenced either. We thus expect no significant impact of a bcc-to-fcc transition within SIW on planetary interiors of Uranus or Neptune.

VI. SUMMARY AND CONCLUSIONS

We have constructed analytic free-energy functions $f(\varrho, T)$ for two phases of SIW (bcc and fcc) by fitting pressures and internal energies from *ab initio* simulations and calculating the entropy. Their primary purpose is to serve in the construction of thermodynamically consistent multiphase EOS tables. These functions are of very high fidelity within the $p - T$ conditions, which the underlying EOS data from FT-DFT-MD simulations were generated for; see Fig. 4. Moreover, they can be extrapolated sufficiently far enough beyond those regions so that boundaries to neighboring phases can be calculated, which was demonstrated in the case of ices VII* and X.

The resolution of transitions between two phases that have very little differences in their thermodynamic functions, like bcc and fcc SIW, remains challenging though. One can imagine that bcc and fcc are not the only possibilities, and that many phases of SIW with low-symmetry oxygen lattices [77] can be simulated dynamically stable with FT-DFT-MD as well. However, for practical applications it does not matter much whether the EOS of the "truly" stable phase or that of a very similar one is used. Although not discussed here in detail, the choice of the exchange-correlation functional has a larger influence on $p(\varrho, T)$ than the type of the oxygen lattice. It is therefore very reasonable to recommend the use of $f(\varrho, T)$ for bcc SIW solely as a good overall representation for the thermodynamics of SIW up to densities of 15 g/cm^3.

Moreover, we showed that the type of the oxygen lattice does not significantly influence the diffusion coefficient of the protons, in contrast to the claims of Wilson *et al.* [15]. Thus, we do not expect any relevant implication for the magnetic field generation in water-rich giant planets that might be caused by transitions between different superionic structures.

Future work will aim at describing the fluid phase in a similar manner and calculating the melt boundary of the superionic structures. Moreover, the techniques developed in this work can be directly applied to investigate superionic and fluid phases of more complex materials, e.g., astrophysically relevant mixtures of hydrogen, helium, oxygen, nitrogen, and carbon [78–80].

ACKNOWLEDGMENTS

This work was supported by the Deutsche Forschungsgemeinschaft (DFG) within the SFB 652 and the SPP 1488. The *ab initio* calculations were performed at the North-German Supercomputing Alliance (HLRN) facilities and at the IT- and Media Center of the University of Rostock. Sandia National Laboratories is a multiprogram laboratory managed and operated by Sandia Corporation, a wholly owned subsidiary of Lockheed Martin Corporation, for the U.S. Department of Energys National Nuclear Security Administration under Contract No. DE-AC04-94AL85000.

[1] T. Encrenaz, Annu. Rev. Astron. Astrophys. **46**, 57 (2008).

[2] I. Baraffe, G. Chabrier, and T. Barman, Rep. Prog. Phys. **73**, 016901 (2010).

[3] C. Arridge, N. Achilleos, J. Agarwal, C. Agnor, R. Ambrosi, N. André, S. Badman, K. Baines, D. Banfield, M. Barthélémy, M. Bisi, J. Blum, T. Bocanegra-Bahamon, B. Bonfond, C. Bracken, P. Brandt, C. Briand, C. Briois, S. Brooks, J. Castillo-Rogez, T. Cavalié, B. Christophe, A. Coates, G. Collinson, J. Cooper, M. Costa-Sitja, R. Courtin, I. Daglis, I. de Pater, M. Desai, D. Dirkx, M. Dougherty, R. Ebert, G. Filacchione, L. Fletcher, J. Fortney, I. Gerth, D. Grassi, D. Grodent, E. Grün, J. Gustin, M. Hedman, R. Helled, P. Henri, S. Hess, J. Hillier, M. Hofstadter, R. Holme, M. Horanyi, G. Hospodarsky, S. Hsu, P. Irwin, C. Jackman, O. Karatekin, S. Kempf, E. Khalisi, K. Konstantinidis, H. Krüger, W. Kurth, C. Labrianidis, V. Lainey, L. Lamy, M. Laneuville, D. Lucchesi, A. Luntzer, J. MacArthur, A. Maier, A. Masters, S. McKenna-Lawlor, H. Melin, A. Milillo, G. Moragas-Klostermeyer, A. Morschhauser, J. Moses, O. Mousis, N. Nettelmann, F. Neubauer, T. Nordheim, B. Noyelles, G. Orton, M. Owens, R. Peron, C. Plainaki, F. Postberg, N. Rambaux, K. Retherford, S. Reynaud, E. Roussos, C. Russell, A. Rymer, R. Sallantin, A. Sánchez-Lavega, O. Santolik, J. Saur, K. Sayanagi, P. Schenk, J. Schubert, N. Sergis, E. Sittler, A. Smith, F. Spahn, R. Srama, T. Stallard, V. Sterken, Z. Sternovsky, M. Tiscareno, G. Tobie, F. Tosi, M. Trieloff, D. Turrini, E. Turtle, S. Vinatier, R. Wilson, and P. Zarka, Planet. Space Sci. **104, Part A**, 122 (2014).

[4] A. Masters, N. Achilleos, C. B. Agnor, S. Campagnola, S. Charnoz, B. Christophe, A. Coates, L. Fletcher, G. Jones, L. Lamy, F. Marzari, N. Nettelmann, J. Ruiz, R. Ambrosi, N. Andre, A. Bhardwaj, J. Fortney, C. Hansen, R. Helled, G. Moragas-Klostermeyer, G. Orton, L. Ray, S. Reynaud, N. Sergis, R. Srama, and M. Volwerk, Planet. Space Sci. **104, Part A**, 108 (2014).

[5] V. N. Zharkov and V. P. Trubitsyn, *Physics of Planetary Interiors* (Parchart, Tucson, 1978).

[6] W. B. Hubbard, Science **214**, 145 (1981).

[7] J. J. Fortney and N. Nettelmann, Space Sci. Rev. **152**, 423 (2010).

[8] R. Redmer, T. R. Mattsson, N. Nettelmann, and M. French, Icarus **211**, 798 (2011).

[9] N. Nettelmann, R. Helled, J. Fortney, and R. Redmer, Planet. Space Sci. **77**, 143 (2013).

[10] B. Y. Tian and S. Stanley, Astrophys. J. **768**, 156 (2013).

[11] C. Cavazzoni, G. L. Chiarotti, S. Scandolo, E. Tosatti, M. Bernasconi, and M. Parrinello, Science **283**, 44 (1999).

[12] N. Goldman, L. E. Fried, I. Feng W. Kuo, and C. J. Mundy, Phys. Rev. Lett. **94**, 217801 (2005).

[13] T. R. Mattsson and M. P. Desjarlais, Phys. Rev. Lett. **97**, 017801 (2006).

[14] M. French, T. R. Mattsson, N. Nettelmann, and R. Redmer, Phys. Rev. B **79**, 054107 (2009).

[15] H. F. Wilson, M. L. Wong, and B. Militzer, Phys. Rev. Lett. **110**, 151102 (2013).

[16] A. F. Goncharov, N. Goldman, L. E. Fried, J. C. Crowhurst, I. Feng W. Kuo, C. J. Mundy, and J. M. Zaug, Phys. Rev. Lett. **94**, 125508 (2005).

[17] J. F. Lin, E. Gregoryanz, V. V. Struzhkin, M. Somayazulu, H. K. Mao, and R. J. Hemley, Geophys. Res. Lett. **32**, L11306 (2005).

[18] B. Schwager and R. Boehler, High Press. Res. **28**, 431 (2008).

[19] T. Kimura, Y. Kuwayama, and T. Yagi, J. Chem. Phys. **140**, 074501 (2014).

[20] M. Ahart, A. Karandikar, S. Gramsch, R. Boehler, and R. J. Hemley, High Press. Res. **34**, 327 (2014).

[21] E. Sugimura, T. Komabayashi, K. Ohta, K. Hirose, Y. Ohishi, and L. S. Dubrovinsky, J. Chem. Phys. **137**, 194505 (2012).

[22] V. V. Yakushev, V. I. Postnov, V. E. Fortov, and T. I. Yakysheva, JETP **90**, 617 (2000).

[23] R. Chau, A. C. Mitchell, R. W. Minich, and W. J. Nellis, J. Chem. Phys. **114**, 1361 (2001).

[24] M. French, T. R. Mattsson, and R. Redmer, Phys. Rev. B **82**, 174108 (2010).

[25] M. French, S. Hamel, and R. Redmer, Phys. Rev. Lett. **107**, 185901 (2011).

[26] J. Wicht and A. Tilgner, Space Sci. Rev. **152**, 501 (2010).

[27] S.-T. Lin, M. Blanco, and W. A. Goddard, J. Chem. Phys. **119**, 11792 (2003).

[28] P.-K. Lai, C.-M. Hsieh, and S.-T. Lin, Phys. Chem. Chem. Phys. **14**, 15206 (2012).

[29] M. P. Desjarlais, Phys. Rev. E **88**, 062145 (2013).

[30] M. French and R. Redmer, Phys. Rev. B **91**, 014308 (2015).

[31] P. Hohenberg and W. Kohn, Phys. Rev. **136**, B864 (1964).

[32] W. Kohn and L. J. Sham, Phys. Rev. **140**, A1133 (1965).

[33] N. D. Mermin, Phys. Rev. **137**, A1441 (1965).

[34] G. Kresse and J. Hafner, Phys. Rev. B **47**, 558 (1993).

[35] G. Kresse and J. Hafner, Phys. Rev. B **48**, 13115 (1993).

[36] G. Kresse and J. Hafner, Phys. Rev. B **49**, 14251 (1994).

[37] G. Kresse and J. Furthmüller, Phys. Rev. B **54**, 11169 (1996).

[38] J. Hafner, J. Comput. Chem. **29**, 2044 (2008).

[39] J. P. Perdew, K. Burke, and M. Ernzerhof, Phys. Rev. Lett. **77**, 3865 (1996).

[40] A. C. Mitchell and W. J. Nellis, J. Chem. Phys. **76**, 6273 (1982).

[41] G. A. Lyzenga, T. J. Ahrens, W. J. Nellis, and A. C. Mitchell, J. Chem. Phys. **76**, 6282 (1982).

[42] M. D. Knudson, M. P. Desjarlais, R. W. Lemke, T. R. Mattsson, M. French, N. Nettelmann, and R. Redmer, Phys. Rev. Lett. **108**, 091102 (2012).

[43] T. Kimura, N. Ozaki, T. Sano, T. Okuchi, T. Sano, K. Shimizu, K. Miyanishi, T. Terai, T. Kakeshita, Y. Sakawa, and R. Kodama, J. Chem. Phys. **142**, 164504 (2015).

[44] M. French and R. Redmer, J. Phys. Condens. Matter **21**, 375101 (2009).

[45] P. E. Blöchl, Phys. Rev. B **50**, 17953 (1994).

[46] G. Kresse and D. Joubert, Phys. Rev. B **59**, 1758 (1999).

[47] A. Baldereschi, Phys. Rev. B **7**, 5212 (1973).

[48] H. J. Monkhorst and J. D. Pack, Phys. Rev. B **13**, 5188 (1976).

[49] S. Nosé, J. Chem. Phys. **81**, 511 (1984).

[50] W. G. Hoover, Phys. Rev. A **31**, 1695 (1985).

[51] P. H. Berens, D. H. J. Mackay, G. M. White, and K. R. Wilson, J. Chem. Phys. **79**, 2375 (1983).

[52] G. Robert, P. Legrand, P. Arnault, N. Desbiens, and J. Clérouin, Phys. Rev. E **91**, 033310 (2015).

[53] N. F. Carnahan and K. E. Starling, J. Chem. Phys. **53**, 600 (1970).

[54] J. A. Tjon, Phys. Rev. **143**, 259 (1966).

[55] B. J. Berne, J. P. Boon, and S. A. Rice, J. Chem. Phys. **45**, 1086 (1966).

[56] K. S. Singwi and M. P. Tosi, Phys. Rev. **157**, 153 (1967).

[57] A δ-like memory function instead reproduces the relaxation time approximation.

[58] M. J. Gillan, D. Alfe, J. Brodholt, L. Vocadlo, and G. D. Price, Rep. Prog. Phys. **69**, 2365 (2006).
[59] H. F. Wilson and B. Militzer, Astrophys. J. **745**, 54 (2012).
[60] D. C. Wallace, *Statistical Physics of Crystals and Liquids* (World Scientific, Singapore, 2002).
[61] M. Bethkenhagen, M. French, and R. Redmer, J. Chem. Phys. **138**, 234504 (2013).
[62] M. French and T. R. Mattsson, J. Appl. Phys. **116**, 013510 (2014).
[63] A. Becker, W. Lorenzen, J. J. Fortney, N. Nettelmann, M. Schöttler, and R. Redmer, Astrophys. J. Suppl. Ser. **215**, 21 (2014).
[64] D. Cebulla and R. Redmer, Phys. Rev. B **89**, 134107 (2014).
[65] M. French and T. R. Mattsson, Phys. Rev. B **90**, 165113 (2014).
[66] M. Schöttler, R. Redmer, and M. French, Contrib. Plasma Phys. **53**, 336 (2013).
[67] N. Goldman, E. J. Reed, and L. E. Fried, J. Chem. Phys. **131**, 204103 (2009).
[68] This would require the calculation of a density derivative of the spectra $S_\alpha(\nu)$.
[69] M. Benoit, M. Bernasconi, P. Focher, and M. Parrinello, Phys. Rev. Lett. **76**, 2934 (1996).
[70] B. Militzer and H. F. Wilson, Phys. Rev. Lett. **105**, 195701 (2010).
[71] M. Ji, K. Umemoto, C.-Z. Wang, K.-M. Ho, and R. M. Wentzcovitch, Phys. Rev. B **84**, 220105 (2011).
[72] Y. Wang, H. Liu, J. Lv, L. Zhu, H. Wang, and Y. Ma, Nat. Commun. **2**, 563 (2011).
[73] J. M. McMahon, Phys. Rev. B **84**, 220104 (2011).
[74] A. Hermann, N. W. Ashcroft, and R. Hoffmann, Proc. Natl. Acad. Sci. USA **109**, 745 (2012).
[75] C. J. Pickard, M. Martinez-Canales, and R. J. Needs, Phys. Rev. Lett. **110**, 245701 (2013).
[76] *Metal-to-Nonmetal Transitions*, edited by R. Redmer, F. Hensel, and B. Holst (Springer, Heidelberg, 2010).
[77] J. Sun, B. K. Clark, S. Torquato, and R. Car, Nat. Commun. **6**, 8156 (2015).
[78] R. Chau, S. Hamel, and W. J. Nellis, Nat. Commun. **2**, 203 (2011).
[79] M. Bethkenhagen, D. Cebulla, R. Redmer, and S. Hamel, J. Phys. Chem. A **119**, 10582 (2015).
[80] E. R. Meyer, C. Ticknor, M. Bethkenhagen, S. Hamel, R. Redmer, J. D. Kress, and L. A. Collins, J. Chem. Phys. **143**, 164513 (2015).